

Manipulation and Characterization of Aperiodical Graphene Structures Created in a Two-Dimensional Electron Gas

Shiyong Wang,¹ Liang Z. Tan,² Weihua Wang,¹ Steven G. Louie,^{2,3} and Nian Lin^{1,*}

¹*Department of Physics, The Hong Kong University of Science and Technology, Hong Kong, China*

²*Department of Physics, University of California, Berkeley, California 94720-7300, USA and Material Sciences Division, Lawrence Berkeley National Laboratory, Berkeley, California 94720, USA*

³*Institute for Advanced Study, Hong Kong University of Science and Technology, Hong Kong, China*

(Received 23 October 2013; revised manuscript received 27 August 2014; published 7 November 2014)

We demonstrate that Dirac fermions can be created and manipulated in a two-dimensional electron gas (2DEG). Using a cryogenic scanning tunneling microscope, we arranged coronene molecules one by one on a Cu(111) surface to construct artificial graphene nanoribbons with perfect zigzag (ZGNRs) or armchair edges and confirmed that new states localized along the edges emerge only in the ZGNRs. We further made and studied several typical defects, such as single vacancies, Stone-Wales defects, and dislocation lines, and found that all these defects introduce localized states at or near the Dirac point in the quasiparticle spectra. Our results confirm that artificial systems built on a 2DEG provide rigorous experimental verifications for several long-sought theoretical predictions of aperiodic graphene structures.

DOI: 10.1103/PhysRevLett.113.196803

PACS numbers: 73.20.At, 31.15.ae, 68.37.Ef, 73.63.Kv

The tremendous efforts devoted to graphene research in the past few years have uncovered numerous extraordinary physical and chemical properties of this material [1–4]. In reality, graphene samples always contain defects that significantly alter graphene's intrinsic properties. Aperiodic structures in which the periodic, hexagonal symmetry is disrupted may bestow new properties and functionalities that are absent in the pristine graphene [5–7]. A famous example is graphene nanoribbons with zigzag edges (ZGNRs)—a structure possessing spin-polarized metallic edge states [8–10]. Other examples include localized states associated with point defects [11–13], band gap opening in graphene nanoribbons (GNRs) [14–16], and metallic channels provided by defect lines [17,18], to name a few. Since these new properties may be useful in applications in electronics, chemical reactivity, optical response, and spintronics, it has become a major interest to understand the nature of various types of defects. As compared to the numerous theoretical works, experimental studies of the electronic structures of graphene with aperiodic structures are fewer since it is extremely challenging to fabricate samples with well-defined defects while characterizing the electronic structures locally at the defects. Scanning tunneling microscopy (STM) and spectroscopy were used to probe the local density of states of point defects and various edges [19–27]. Detecting the predicated edge states of narrow ZGNRs with atomically sharp and perfect zigzag edges is yet to be achieved. Since the nature of the edge states may depend sensitively on edge morphology, the lack of GNR samples with perfect zigzag edges has hindered the rigorous verification of the theoretical predictions.

Here we demonstrate that various graphene aperiodic structures including GNRs with homogenous and perfect

zigzag or armchair edges (AGNRs), single vacancy (SV), or Stone-Wales (SW) defects and dislocation lines can be created by low-temperature STM manipulation of coronene [top inset in Fig. 1(a)] molecules on a Cu(111) surface inspired by theory [28] and the pioneering work of Gomes *et al.* [29]. We resolved localization of the edge or point defect states at one of the two sublattices, and the sublattice-specific exponential decay. Our results demonstrate a high degree of control over an artificial graphene system that is not possible in real graphene.

Coronene molecules were deposited on a Cu(111) sample held at room temperature. After 120 °C annealing, the coronene molecules are randomly distributed on the Cu(111) surface at 4.8 K. Figure 1(a) shows a triangular array constructed by manipulating 300 coronene molecules with an intermolecular distance of 2.7 nm. Subjected to the repulsive potential provided by the coronene molecules, the two-dimensional electron gas (2DEG) provided by the Cu(111) surface state electrons are confined in the channels of a honeycomb network. The center of the triangle formed by three neighboring molecules can be viewed as the atomic site of the graphene structure, whereas the middle bridges between two adjacent molecules correspond to the “bonds” of the graphene structure. Figure 1(b) shows a tunneling spectrum averaged over the artificial graphene, which corresponds to the density of states (DOS). The V-shape DOS is a manifestation of massless Dirac fermions [28–30]. The bottom of the V, the Dirac point, is at 0.23 V below the Fermi level, and is 0.17 V above the onset of the Cu(111) surface-state band that forms the 2DEG. Furthermore, we resolved the quasiparticle band dispersion using Fourier-transformed scanning tunneling spectroscopy (FTLDOS); for detail see the Supplemental

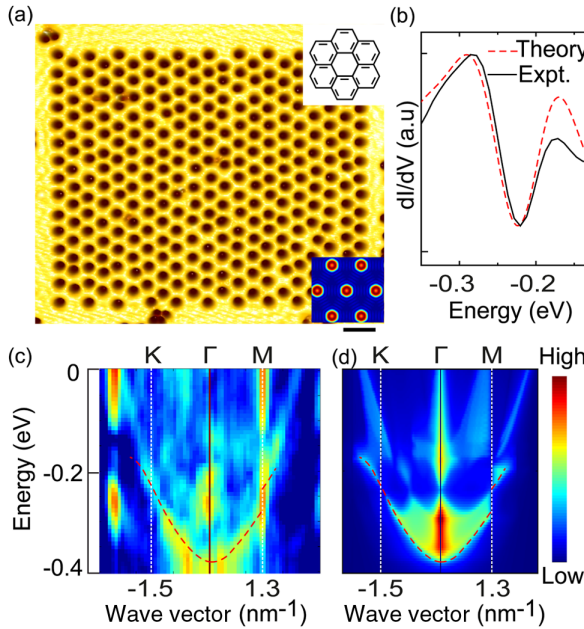


FIG. 1 (color online). (a) STM image of an artificial pristine graphene structure of a triangular array consisting of 300 coronene molecules. Top inset: chemical structure of coronene; bottom inset: simulation model (the red discs are 1.0 eV potentials). Scale bar: 5 nm. (b) Experimental dI/dV (solid) and simulated DOS spectrum (dashed). (c) Power function along ΓK (left) and ΓM (right) directions resolved by 2D FTLDOS. Dashed curves are simulated band dispersions along the defined directions. (d) Simulated FTLDOS.

Material [31]. Figure 1(c) shows the power functions in the ΓK (left) and ΓM (right) directions. At -0.23 eV, the band structure can be described by a Dirac cone at the K and K' points of the Brillouin zone. Scattering between these Dirac cones gives rise to characteristic features in the FTLDOS spectrum along the ΓK and ΓM directions. We have calculated the band structure by treating the system as a noninteracting 2DEG in a triangular array of repulsive potential disks as illustrated in the inset of Fig. 1(a) [32]. The potential is set as 1.0 eV, the muffin-tin radius is 0.7 nm, and the effective mass of the Cu surface-state band is $0.4m_e$. The calculated DOS and FTLDOS are plotted in Figs. 1(b) and 1(d), respectively. One can see that experiment and theory agree very well [note the dashed curves in Figs. 1(c) and 1(d) highlight the intensity of the calculated FTLDOS]. The Fermi velocity obtained from the band structure is 2.6×10^5 m/s. Note the different potential profiles of the coronene molecules used in our work and the CO molecules used in Ref. [29] should also lead to some differences in the electronic structure of various defects, such as the energy of the defect state or the size of the band gaps, etc.

Termination of the infinite graphene sheet results in edge(s). Ideal GNRs should have two parallel edges. We constructed artificial GNRs of specific configurations. The

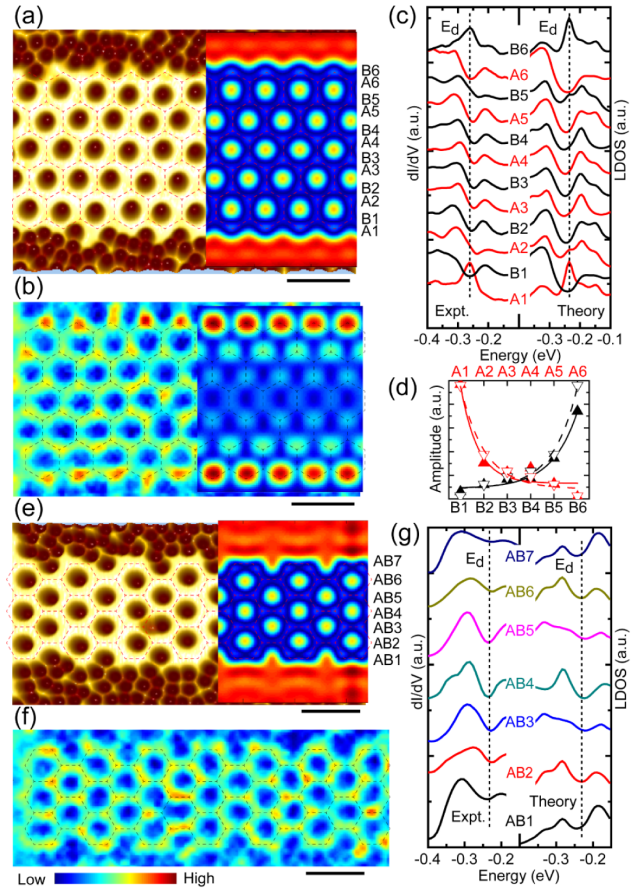


FIG. 2 (color online). (a)–(d) An artificial 6-ZGNR. (a) STM image (left part) and simulation model (right part). (b) STS map acquired at -0.26 V (left part) and simulated LDOS map at -0.24 V (right part). (c) Experimental row-averaged dI/dV spectra and calculated LDOS. Black dashed line indicates the Dirac point. (d) The amplitude of the edge state (We use the term “amplitude of the edge state” to refer to the modulus squared of the wave function in the calculation, and to the dI/dV value at the position and bias voltage of the edge state in the experiment.) as a function of row index. Experimental (calculated) results are shown in solid (open) symbols. (e)–(g) An artificial 7-AGNR. (e) STM image (left part) and simulation model (right part). (f) STS map acquired at -0.23 V. (g) Experimental row-averaged dI/dV spectra and calculated LDOS. Scale bars: 5 nm.

left part of Fig. 2(a) shows a section of a 6-ZGNR (the full length of the ZGNR is about 4 times longer containing 40 repeated units and we only consider the data in the middle part in order to minimize the end effects), where the dashed lines are guides for the eye. Since the 2DEG outside the GNR region is depleted by the close-packed molecules, this structure can be viewed as a ZGNR. We define that the bottom edge is of sublattice A and the top edge is of sublattices B, and different rows are numbered from 1 to 6. Row-averaged local density of states (LDOS) acquired at the defined rows are plotted in Fig. 2(c). Both edge rows (A_1 and B_6) have a pronounced peak emerging at the Dirac point as marked by the dashed line. The amplitude of the

new state as a function of row index is displayed in Fig. 2(d). The amplitude decays in the interior of the ribbon, indicating the state is localized at the two edges. Interestingly, the two sublattices behave independently and each one can be fitted by an exponential function $e^{-L/\xi}$ with a decay constant $\xi = 1.1a_0$ ($1.6a_0$) for the A (B) sublattice, where a_0 is the artificial bond length. The localization of the state is apparent in the LDOS map, as shown in the left part of Fig. 2(b), which was acquired at the energy of the edge states (-0.26 V). One can see that the high intensity spots are at the lattice sites of the two edges ($A1$ or $B6$). All these features are consistent with the predictions [8–10,14]. We simulated a 6-ZGNR shown in the right part of Fig. 2(a). (The calculated quasiparticle band structure is shown in the Supplemental Material [31].) The simulated row-averaged LDOS, as shown in Fig. 2(c), manifest states (marked by the dashed line) at -0.24 V whose intensity is maximum at the two edges and decays in the interior. The decay trend is plotted in Fig. 2(d), which can be fitted by an exponential function with a decay constant of $1.6a_0$. The simulated real-space LDOS map at -0.24 V shown in the right part of Fig. 2(b) further reveals the spatial localization of these states along the two edges. In our measurements, we do not observe any splitting of the edge states arising from magnetic effects [14]; we neglect such effects in our simulations. Overall, the simulation nicely reproduces the characteristics of the experimentally resolved edge states. We also constructed a 4-ZGNR and a 2-ZGNR and found both structures have states that are localized at the two edges (see Supplemental Material [31]). The single-sublattice behavior of the zero-energy (relative to the Dirac point) edge states of the ZGNRs can be understood by considering the appropriate boundary conditions in $\vec{k} \cdot \vec{p}$ perturbation theory [33]. On a single zigzag edge, the terminal honeycomb sites all belong to a single (B) sublattice. The wave function should vanish on the A sites exterior to the ribbon that are adjacent to these terminal B sites. Furthermore, for the zero energy states, the $\vec{k} \cdot \vec{p}$ wave function should vanish on all interior A sites as well [33]. The 558 line defect and single vacancy structures we have constructed further illustrate this principle.

For comparison, we constructed a system not expected to show such single-sublattice behavior: an artificial 7-AGNR as shown in the left part of Fig. 2(e). Row-averaged DOS acquired at the defined rows are displayed in Fig. 2(g). In clear contrast to the ZGNRs, the AGNR does not have any edge states near the Dirac point energy. Figure 2(f) shows a STS map acquired at -0.24 V, which reveals that the states are distributed in the entire ribbon. We simulated the artificial 7-AGNR [right part of Fig. 2(f)] (the calculated quasiparticle band structure is shown in the Supplemental Material [31]). As shown in Fig. 2(g), the simulated DOS exhibit comparable features as the experimental ones: a dip at -0.24 V and the absence of any localized edge state. In conclusion, both experimental observations and theoretical

simulations confirm that the artificial AGNR does not have the edge states.

Now we turn our focus to the line defect. A widely studied topological line defect consists of repeating paired pentagons fused with octagons, named as the 558 line defect [11]. Recently, Lahiri *et al.* [18] reported on an experimental observation of this type of line defect when growing graphene on a Ni substrate. The DFT calculation predicted the existence of metallic states that are localized at the line defect [18]. We made an artificial structure which represents an analogue of the 558 line defect. Starting from a perfect triangular coronene molecular structure, we shifted the molecules of the two neighboring columns in a way that four neighboring molecules were pushed together while the molecules in the upper and lower rows were separated apart. This process was repeated along the entire column. Figure 3(a) (upper panel) shows a section of the artificial defect line (the full length is 4 times larger), where a structural model of the 558 line defect is sketched. We define the center of the two columns as the defect line (DL) and different columns as A^L_n , B^L_n , A^R_n , B^R_n ,

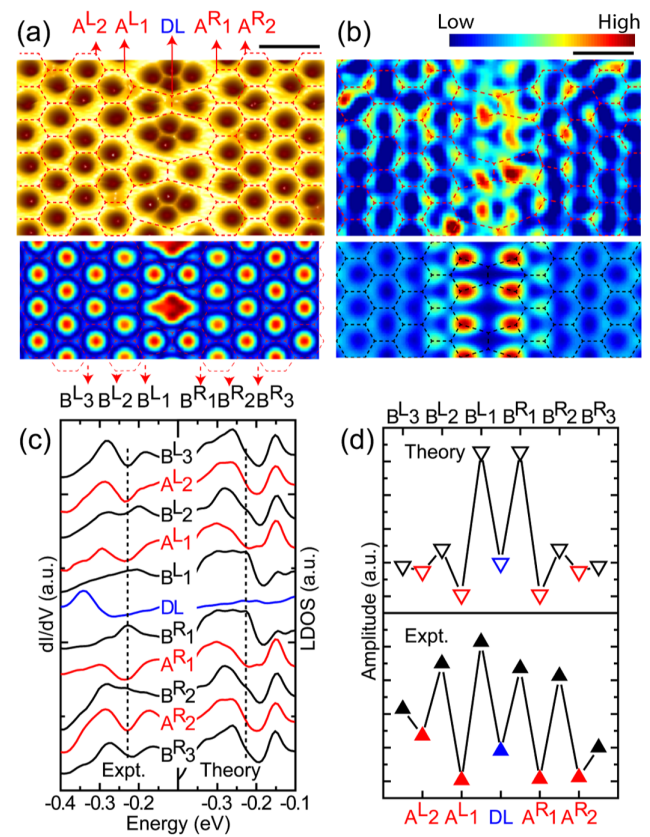


FIG. 3 (color online). (a) STM image (upper) and simulation model (lower) of an artificial 558 defect line. (b) STS map acquired at -0.23 V (upper) and simulated LDOS map at -0.21 V (lower). (c) Experimental column-averaged dI/dV spectra and calculated LDOS. (d) Calculated LDOS intensity (upper) measured LDOS amplitude (lower) at -0.22 V as a function of column index. Scale bars: 5 nm.

respectively, where A (B) stands for a sublattice, L (R) for a column to the left (right) of the DL, and n the distance index. Column-averaged LDOS acquired at the defined columns are plotted in Fig. 3(c). One can see that the V-shape dip disappears at the DL. Interestingly, the spectra at B^L_1 and B^R_1 show a peak at -0.23 V, which indicates that there are new states emerging at the Dirac point at the B sublattice. In contrast, the new states are absent at the A sublattice. Figure 3(d) (lower panel) displays the measured dI/dV amplitude at -0.23 V as a function of the column index, manifesting (1) the new states are absent in the DL or the A sublattice, (2) in the B sublattice, the amplitude decays away from the DL. In the upper panel of Fig. 3(b), a DOS map acquired at -0.23 V reveals that the new states are confined within four lattice sites in the vicinity of the DL. We simulated the artificial 558 line defect [Fig. 3(a), lower part]. The calculated column-averaged LDOS spectra are shown in Fig. 3(c) (the calculated quasiparticle band structure is shown in the Supplemental Material [31]). Similar to the experimental observation, at -0.21 V, a new state emerges at the B sublattice only but is absent at the A sublattice. As shown in the upper panel of Fig. 3(d), away from the DL the amplitudes of the new state at the B sublattice decays exponentially. A LDOS map of -0.21 V is shown in the lower panel of Fig. 3(b), which reproduces the localization characteristics observed in the experiment. These results confirm that the 558 line defect exhibits states near the Dirac point along the line and, in particular, the state is only present at the sublattice which borders the line defect.

In the last part, we present the results of two basic types of intrinsic point defects—single vacancies and Stone-Wales defects. It was shown theoretically that vacancies induce quasilocalized states at the Fermi level if the intrinsic electronic structure shows electron-hole symmetry [6]. Experimentally, STM revealed that single vacancies on a graphite surface can introduce a sharp electronic resonance at the Fermi energy around each single graphite vacancy [19–21]. Here, we created a structure by inserting an extra coronene molecule at the center of three adjacent coronene molecules in a regular array. As shown in Fig. 4(a), the extra molecule occupies a lattice site in the honeycomb structure. Since this molecule provides a repulsive potential, this site becomes a barrier for the 2D surface electrons, so this structure can be viewed as an artificial missing-atom defect. We measured the LDOS at the sites that are in specific distance to the defect denoted as A_n or B_n , where A (B) stands for the A (B) sublattice (note the vacancy is at sublattice B) and n the distance index ($n = 1$ defines the three nearest sites). As shown in the left panel of Fig. 4(b), the two sublattices exhibit very different characters: a measured peak (-0.23 V) appears near the Dirac point only at A sites, while the B sites show a V-shape dip. In accordance with the breaking of the A - B sublattice symmetry, the measured dI/dV map [upper panel of Fig. 4(c)] taken at -0.23 V shows that the new state

appears at the A sublattice sites only. The dI/dV map further reveals that the new state is localized around the vacancy. To resolve the spatial localization quantitatively, we averaged the spectra of the equivalent sites of A_n and B_n in all radial directions originated from the defect. The results are summarized in Fig. 4(d). One can find two interesting features: (i) the intensity of the new states at A sites decays exponentially, which can be fitted by an exponential function with a decay constant of $1.2a_0$; (ii) the intensity is low at B sites and increases slightly away from the vacancy. The symmetry breaking becomes insignificant beyond the 10th lattice site. All these features are explained and quantitatively reproduced by theory as seen in Fig. 4.

The Stone-Wales (SW) defect represents the simplest example of topological defects, in which four hexagons are transformed into two pentagons and two heptagons by rotating a C-C bond by 90° [5,12,13,34]. This type of defect does not have dangling bonds, but they were predicted to scatter the electron waves strongly and hence have a drastic influence on the electrical transport properties [7]. We made an artificial SW defect by relocating four adjacent coronene molecules that are in orthogonal positions as shown in Fig. 4(e). We found that this structure also exhibits a pronounced peak near the Dirac point (-0.23 V), as revealed by the site-specific dI/dV acquired at one of the pentagons as shown in the left panel of Fig. 4(f). For reference, the dI/dV acquired at the black dot in Fig. 4(e) is also plotted, showing a normal V-shape dip. Figure 4(g) (left panel) is a -0.23 V dI/dV map which manifests that the new states are spatially localized at the two pentagons. We also made several defects with other

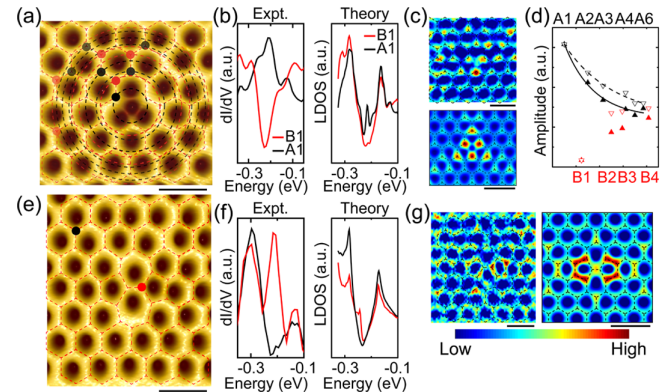


FIG. 4 (color online). (a)–(d) An artificial single vacancy. (a) STM image. (b) Experimental (left) and simulated (right) dI/dV spectra acquired at sites A_1 and B_1 [marked as the black and red dots in (a)]. (c) Experimental (upper) and simulated (lower) dI/dV maps at -0.23 V. (d) Experimental (solid) and simulated (open) -0.23 V LDOS amplitude as a function of sites. (e)–(g) An artificial Stone-Wales defect. (e) STM image. (f) Experimental (left) and simulated (right) dI/dV spectra (Red: acquired with the tip located at the red dot marked in (e); Black: from the unmodified sites). (g) Experimental (left) and simulated (right) dI/dV maps at -0.23 V. Scale bars: 5 nm.

configurations (see the Supplemental Material [31]). In all these examples, we found that emergence of the localized states near the Dirac point is a general phenomenon. We simulated the artificial single vacancy and the SW defects. The results, as shown in Figs. 4(b)–4(d), 4(f), and 4(g), reproduce the experimentally obtained features qualitatively. The defect state decays exponentially with a decay length of $2.1a_0$. The discrepancies of the simulation and the experiment presumably are caused by the simplicity of the muffin-tin type potential used in the simulation.

We expect that the strategy used in this work may be able to create nontrivial states such as 2D topological insulators using potentials with magnetic moment or modulating the surface states that have a strong spin-orbit coupling [35].

This work is supported by the Hong Kong RGC (No. 602712), the National Science Foundation Grant No. DMR 10-1006184 and by the Director, Office of Science, Office of Basic Energy Sciences, Material Sciences and Engineering Division, U.S. Department of Energy under Contract No. DE-AC02-05CH11231. S. G. L. acknowledges support from a Simons Foundation Fellowship in Theoretical Physics. We acknowledge the assistance of the XSEDE computational cluster resource provided by NICS (Kraken), supported by the National Science Foundation.

*To whom all correspondence should be addressed.
phnlin@ust.hk

- [1] K. S. Novoselov *et al.*, *Science* **306**, 666 (2004).
- [2] K. S. Novoselov, A. K. Geim, S. V. Morozov, D. Jiang, M. I. Katsnelson, I. V. Grigorieva, S. V. Dubonos, and A. A. Firsov, *Nature (London)* **438**, 197 (2005).
- [3] A. H. C. Neto, F. Guinea, N. M. R. Peres, K. S. Novoselov, and A. K. Geim, *Rev. Mod. Phys.* **81**, 109 (2009).
- [4] A. K. Geim, *Science* **324**, 1530 (2009).
- [5] F. Banhart, J. Kotakoski, and A. V. Krasheninnikov, *ACS Nano* **5**, 26 (2011).
- [6] V. M. Pereira, F. Guinea, J. M. B. Lopes dos Santos, N. M. R. Peres, and A. H. Castro Neto, *Phys. Rev. Lett.* **96**, 036801 (2006).
- [7] O. V. Yazyev and S. G. Louie, *Phys. Rev. B* **81**, 195420 (2010).
- [8] M. Fujita, K. Wakabayashi, K. Nakada, and K. Kusakabe, *J. Phys. Soc. Jpn.* **65**, 1920 (1996).
- [9] K. Nakada, M. Fujita, G. Dresselhaus, and M. S. Dresselhaus, *Phys. Rev. B* **54**, 17954 (1996).
- [10] Y.-W. Son, M. L. Cohen, and S. G. Louie, *Nature (London)* **444**, 347 (2006).
- [11] R. Faccio, L. Fernández-Werner, H. Pardo, C. Goyenola, O. N. Ventura, and Á. W. Mombrú, *J. Phys. Chem. C* **114**, 18 961 (2010).
- [12] J. Ma, D. Alfé, A. Michaelides, and E. Wang, *Phys. Rev. B* **80**, 033407 (2009).
- [13] E. J. Duplock, M. Scheffler, and P. J. D. Lindan, *Phys. Rev. Lett.* **92**, 225502 (2004).
- [14] Y.-W. Son, M. L. Cohen, and S. G. Louie, *Phys. Rev. Lett.* **97**, 216803 (2006).
- [15] S. Dutta and S. K. Pati, *J. Mater. Chem.* **20**, 8207 (2010).
- [16] M. Y. Han, B. Ozylmaz, Y. B. Zhang, and P. Kim, *Phys. Rev. Lett.* **98**, 206805 (2007).
- [17] E. Cockayne, G. M. Rutter, N. P. Guisinger, J. N. Crain, P. N. First, and J. A. Stroscio, *Phys. Rev. B* **83**, 195425 (2011).
- [18] J. Lahiri, Y. Lin, P. Bozkurt, I. I. Oleynik, and M. Batzill, *Nat. Nanotechnol.* **5**, 326 (2010).
- [19] M. M. Ugeda, I. Brihuega, F. Guinea, and J. M. Gómez-Rodríguez, *Phys. Rev. Lett.* **104**, 096804 (2010).
- [20] M. M. Ugeda, D. Fernández-Torre, I. Brihuega, P. Pou, A. J. Martínez-Galera, R. Pérez, and J. M. Gómez-Rodríguez, *Phys. Rev. Lett.* **107**, 116803 (2011).
- [21] M. M. Ugeda, I. Brihuega, F. Hiebel, P. Mallet, J.-Y. Veuillet, J. M. Gómez-Rodríguez, and F. Ynduráin, *Phys. Rev. B* **85**, 121402 (2012).
- [22] C. Tao *et al.*, *Nat. Phys.* **7**, 616 (2011).
- [23] Y. Kobayashi, K. I. Fukui, T. Enoki, and K. Kusakabe, *Phys. Rev. B* **73**, 125415 (2006).
- [24] K. A. Riter and J. W. Lyding, *Nat. Mater.* **8**, 235 (2009).
- [25] M. Pan, E. Costa Girão, X. Jia, S. Bhaviripudi, Q. Li, J. Kong, V. Meunier, and M. S. Dresselhaus, *Nano Lett.* **12**, 1928 (2012).
- [26] X. Zhang *et al.*, *ACS Nano* **7**, 198 (2013).
- [27] P. Ruffieux *et al.*, *ACS Nano* **6**, 6930 (2012).
- [28] C.-H. Park and S. G. Louie, *Nano Lett.* **9**, 1793 (2009).
- [29] K. K. Gomes, W. Mar, W. Ko, F. Guinea, and H. C. Manoharan, *Nature (London)* **483**, 306 (2012).
- [30] Nadvornik *et al.*, *New J. Phys.* **14**, 053002 (2012).
- [31] See Supplemental Material at <http://link.aps.org/supplemental/10.1103/PhysRevLett.113.196803> for experimental methods, experimental data of a 4-ZGNR, a 2-ZGNR and a defect, and calculated quasiparticle band structures.
- [32] S. Wang, W. Wang, L. Z. Tan, X. G. Li, Z. Shi, G. Kuang, P. N. Liu, S. G. Louie, and N. Lin, *Phys. Rev. B* **88**, 245430 (2013).
- [33] L. Brey and H. A. Fertig, *Phys. Rev. B* **73**, 235411 (2006).
- [34] B. W. Jeong, J. Ihm, and G.-D. Lee, *Phys. Rev. B* **78**, 165403 (2008).
- [35] P. Ghaemi, S. Gopalakrishnan, and T. L. Hughes, *Phys. Rev. B* **86**, 201406 (2012).